JACS
JOURNAL OF THE AMERICAN CHEMICAL SOCIETY
pubs.acs.org/JACS
Article

Ultrafast Ring-Opening Reaction of 1,3-Cyclohexadiene: Identification of Nonadiabatic Pathway via Doubly Excited State

Shutaro Karashima, Alexander Humeniuk, Ryuta Uenishi, Takuya Horio, Manabu Kanno, Tetsuro Ohta, Junichi Nishitani, Roland Mitrić, and Toshinori Suzuki*

Cite This: https://doi.org/10.1021/jacs.1c01896
Read Online
ACCESS | Metrics & More | Article Recommendations | Supporting Information

ABSTRACT: The photoinduced ring-opening reaction of 1,3-cyclohexadiene (CHD) to produce 1,3,5-hexatriene (HT) plays an essential role in the photobiological synthesis of vitamin D_3 in the skin. This reaction follows the Woodward–Hoffmann rule, and C_5–C_6 bond rupture via an electronically excited state occurs with conrotatory motion of the end CH_2 groups. However, it is noted that the photoexcited $S_1(\pi,\pi^*)$ state of CHD is not electronically correlated with the ground state of HT, and the reaction must proceed via nonadiabatic transitions. In the present study, we have clearly observed the nonadiabatic reaction pathway via the doubly excited state of CHD using ultrafast extreme UV photoelectron spectroscopy. The results indicate that the reaction occurs in only 68 fs and creates product vibrational coherence. Extensive computational simulations support the interpretation of experimental results and provide further insights into the electronic dynamics in this paradigmatic electrocyclic ring-opening reaction.

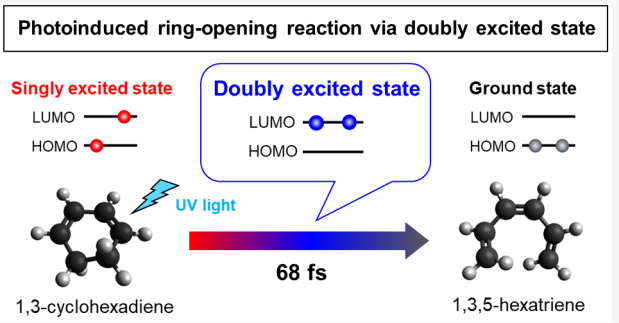

INTRODUCTION

The photoinduced ring-opening reaction of 1,3-cyclohexadiene (CHD) to produce 1,3,5-hexatriene (HT) is a well-known example of electrocyclic chemical reactions,[1] and it plays a central role in the photobiological synthesis of vitamin D_3 in the skin by facilitating photoisomerization of 7-dehydrocholesterol to previtamin D_3. The ring-opening reaction of CHD follows the Woodward–Hoffmann rule, and C_5–C_6 bond rupture via the electronically excited state occurs with conrotatory motion of the end CH_2 groups.[2] The reaction starts from the $S_1(\pi,\pi^*)$ state of CHD reached by a HOMO(π)–LUMO(π^*) transition in the ultraviolet (UV) region, and the photoexcited state ultimately leads to the ground electronic state (S_0) of HT[3] with the quantum yield of approximately 0.5.[4−8] However, it should be noted that the $S_1(\pi,\pi^*)$ state of CHD is not electronically correlated with the S_0 state of HT; therefore, the reaction must be facilitated by nonadiabatic transitions among different electronic states (Figure 1).

The well-known feature of this paradigmatic ring-opening reaction is that the energy ordering of the HOMO(12a) and LUMO(11b) is reversed between the reactant and product. (Here, the notations a and b of the molecular orbital symmetry are the irreducible representations in the C_2 point group. We employ these notations in order to explain the orbital correlation between CHD and HT.) Consequently, the S_0 state of HT with double occupancy of the 11b orbital is correlated with the doubly excited S_2 state of CHD. In the 1960s, van der Lugt and Oosterhoff performed a theoretical analysis of a related ring-closing reaction from butadiene to cyclobutene, and they pointed out that the reaction is mediated by a conical intersection (CoIn) of the potential energy surface with a doubly excited state;[9] the same mechanism has been expected for the ring-opening reaction of CHD. It is noted that the ground state of CHD with the double occupancy of the 12a orbital is electronically correlated with the doubly excited state of HT so that the two potential energy surfaces indicated in black and blue in Figure 1 undergo strong avoided crossing under the C_2 symmetry, making the S_1–S_0 energy gap to be prohibitively large for efficient nonadiabatic transition (it is seen in our ab initio calculations shown in Figure 3). Therefore, the reaction has been predicted to involve the symmetry-breaking nuclear motion to access the S_1/S_0 seam of crossing under non-C_2 symmetry.[10]

Experimental attempts to observe the ring-opening reaction of CHD in real time started decades ago, when Fuß and colleagues[3,11,12] performed ultrafast photoionization mass spectrometry using strong field ionization. Their experimental results inspired a number of subsequent experimental and

Received: February 17, 2021

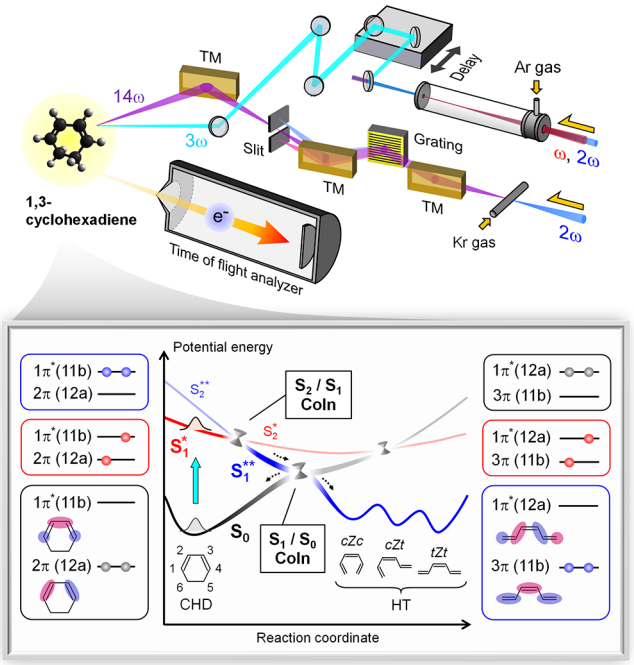

Figure 1. Experimental setup and schematic diagram of ring-opening reaction of CHD. Deep UV pump (3ω, 267 nm, 4.6 eV) and extreme UV probe (14ω, 57 nm, 21.7 eV) pulses were employed (TM, toroidal mirror; CoIn, conical intersection; CHD, 1,3-cyclohexadiene; HT, 1,3,5-hexatriene). The orbital symmetries are indicated assuming the C_2 symmetry to illustrate the correlation of the orbitals between CHD and HT. C_2 symmetry holds only between the Franck–Condon region and S_2/S_1 CoIn. The symmetry-breaking motions play an important role to access the S_1/S_0 seam of crossing under non-C_2 symmetry.

theoretical studies on this reaction.[3−8,10−21] Time-resolved photoelectron spectroscopy (TRPES),[5,18,19] ultrafast near-edge X-ray absorption fine structure spectroscopy[20] and ultrafast electron diffraction experiments[21] have been performed to study the reaction. Nevertheless, the reaction pathway via the doubly excited state has yet to be unambiguously identified. One of the difficulties with these previous experiments was their relatively low temporal resolution. As described in the present paper, the nonadiabatic transition occurs within 30 fs after photoexcitation, and it is therefore crucial to have a sufficiently high time-resolution to clearly capture the nonadiabatic transition. In this regard, the cross-correlation time (typically 100–150 fs) of the pump and probe pulses in past ultrafast spectroscopy experiments on this system was insufficient except for the experiment by Fuß and colleagues using 13 fs pulses.[11] Furthermore, mass spectrometry and X-ray/electron diffraction experiments are generally insensitive to the electronic character of a molecule so that they are not best-suited for observation of nonadiabatic transitions.

The objective of the present study is to perform real-time observation of the electronic dynamics of the ring-opening reaction of CHD and to establish a mechanistic picture of this paradigmatic ring-opening reaction. To this end, TRPES was employed with extreme UV (EUV) probe pulses (21.7 eV).[22] The EUV pulses ionize all the chemical species involved in the reaction;[23] therefore, EUV photoelectron spectroscopy enables complete observation of the dynamics from the Franck–Condon (FC) region in the $S_1(\pi,\pi^*)$ state of CHD until the final states of the reaction products. High temporal resolution of measurements is crucial for clear identification of the reaction path; therefore, a filamentation four-wave mixing (FFWM) deep UV (DUV) light source[24] and a high-order harmonic generation (HHG) EUV light source were combined to achieve their cross-correlation time of 48 ± 2 fs in this study. In Supporting Information section S6, we also present the results obtained using time-resolved photoelectron imaging (TRPEI) with UV pump and vacuum UV (6.3 or 7.4 eV) probe pulses with a shorter cross-correlation time of 31–32 fs, which fully support the results obtained with EUV probe pulses presented below.

In the discussion presented below, we employ the following nomenclature for the electronic states. We consider only the valence singlet states and indicate them with the symbol S_n (n = 0, 1, 2, ...), in which n starts from 0 in ascending order of electronic energy. (The Rydberg states are conventionally neglected in studies of the ring-opening reaction of CHD from the S_1 state because these states play a negligible role.) Furthermore, we use single and double asterisks to indicate predominantly singly and doubly excited electronic characters, respectively. Therefore, when the first excited singlet state with a singly excited electronic character undergoes avoided crossing with the doubly excited electronic state, the notation changes from S_1* to S_1**. We will later discuss the doubly excited electronic characters of the S_1 and S_2 states more fully based on quantum chemical calculations. Since the C_2 symmetry of CHD is lifted during the reaction, we use the irreducible representation in the C_2 point group only when it is indispensable for explaining the character of molecular orbitals and the propensity of electronic transitions. Figure 1 employs both the nomenclature S_n (n = 0, 1, 2, ...) with asterisks and the molecular orbital symmetries under the C_2 symmetry in order to explain the correlation of electronic states between CHD and HT.

RESULTS AND DISCUSSION

Figure 2A shows a two-dimensional (2D) map of EUV photoelectron spectra measured as a function of the pump–probe delay time. The pump pulses excited CHD to the S_1* state, and the EUV probe pulses induced photoemission from all transient species in all electronic states. The spectra are plotted against the electron binding energy (eBE), given by the difference between the EUV photon energy and the measured electron kinetic energy (eKE). The three negative-intensity bands indicated in violet in Figure 2A are the ground-state bleach (depopulation) induced by the UV pump pulses, which can be confirmed by comparing with an EUV photoelectron spectrum of CHD at room temperature shown in the same figure. The positive signals at short pump–probe delay times (<100 fs) are primarily from the excited electronic state of CHD, while those at longer delay times are from the reaction products.

Figure 2B shows an enlarged view of the rectangular region outlined by the white dashed lines in Figure 2A. The photoelectron signal for S_1* starts from three eBE values of 3.8, 6.2, and 7.1 eV at time zero. The lowest eBE band is associated with the $D_0 \leftarrow S_1$* ionization transition; the initial eBE value of 3.8 eV at the time origin agrees well with the vertical ionization energy of CHD of 8.4 eV measured using our apparatus. The photoabsorption spectrum of matrix-isolated CHD^+ cations exhibits two bands at around 2.62 and 3.20 eV,[25] which can be assigned to the first and second

https://doi.org/10.1021/jacs.1c01896
J. Am. Chem. Soc. XXXX, XXX, XXX−XXX

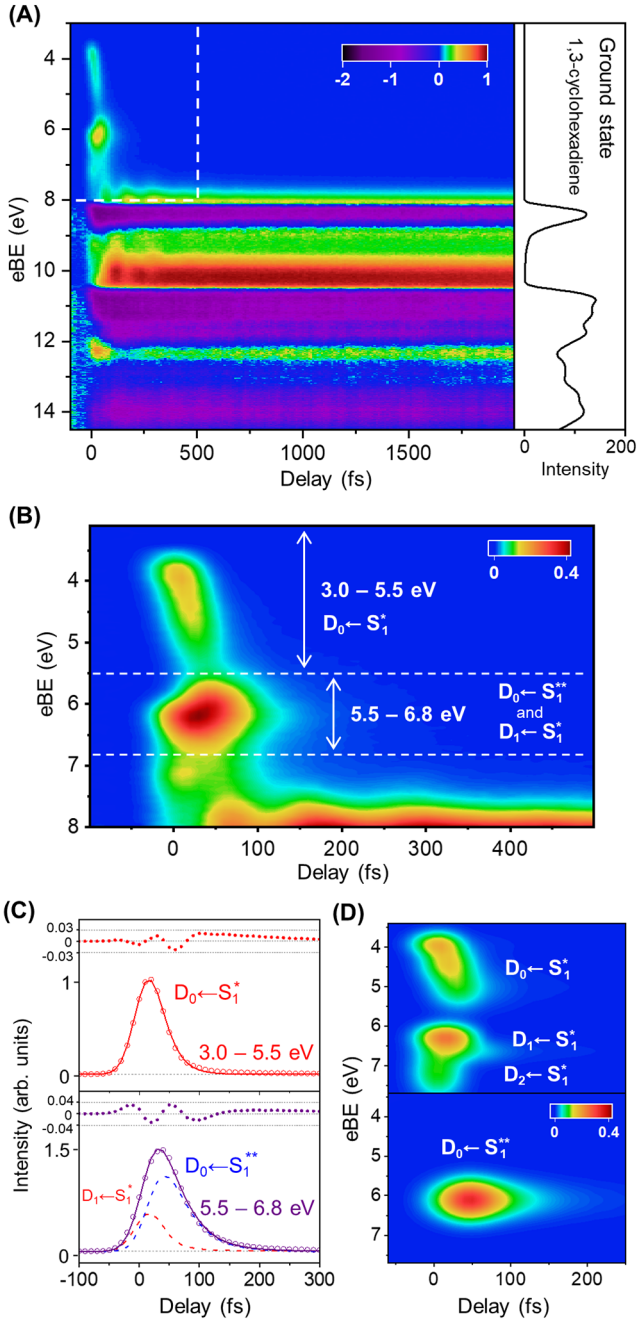

Figure 2. Experimental photoelectron spectra. (A) 2D map of EUV photoelectron spectra with the photoelectron spectrum of the ground-state CHD shown on the right. The negative signals correspond to the ground-state bleach. (B) Enlarged 2D map of the area indicated with dashed lines in (A). (C) Time profiles of the photoelectron signal intensities integrated over 3.0−5.5 and 5.5−6.8 eV regions (open circles) and their least-squares fitting (solid lines). Dashed lines indicate the deconvoluted components of S_1* and S_1**. The residues of the least-squares fitting are shown with dots above the profiles. These time profiles were measured with the experimental uncertainties of 1%. (D) 2D maps of the contributions from S_1* and S_1**. See Supporting Information section S5 for details.

excited cationic states (D_1 and D_2). The observed eBE values of 6.2 and 7.1 eV agree reasonably well with those expected for $D_1 \leftarrow S_1$* and $D_2 \leftarrow S_1$*, respectively. As the delay time is increased, the $D_0 \leftarrow S_1$* band shifts rapidly to higher eBE because the electronic energy of S_1* decreases along the ring-opening reaction path, while the energy of the stable cationic ground state D_0 increases along the path (Figure 4B). The S_1* signal intensity integrated over an energy range of 3.0−5.5 eV, as shown with red open circles in Figure 2C, exhibits a single exponential decay. The time profiles shown in Figure 2C were determined with experimental uncertainties of 1%. As described in Supporting Information section S2, the high fidelity of our measurement enabled estimation of the time constants with a standard deviation of about 10%, which corresponds to several femtoseconds. The profile of S_1* was reasonably well expressed with a latency time and exponential decay time constant of 10 ± 3 and 21 ± 2 fs, respectively, from which the 1/e lifetime of S_1* was determined to be 31 fs. As presented in Supporting Information section S6-2, we also performed TRPEI experiments using vacuum UV pulses, which provided slightly different estimates of the latency time and decay time constant of 17 ± 4 and 17 ± 6 fs, respectively; however, these values also provide an S_1* lifetime of 34 fs. Thus, we conclude that the S_1* population decreases to 1/e in approximately 31−34 fs.

The photoemission band intensity in the next eBE region of 5.5−6.8 eV exhibits different temporal behavior. As shown in Figure 2C, the integrated intensity in this energy range appears time-delayed with respect to the signal in the 3.0−5.5 eV range and decays more slowly. If only the $D_1 \leftarrow S_1$* transition occurs in the 5.5−6.8 eV region, the time profiles observed for the two regions of 3.0−5.5 and 5.5−6.8 eV are expected to be the same. However, the observed difference between the time profiles indicates that another photoemission band corresponding to $D_0 \leftarrow S_1$** transition exists in the 5.5−6.8 eV region. We will confirm this assignment later using quantum chemical calculations. The individual contributions of the $D_1 \leftarrow S_1$* and $D_0 \leftarrow S_1$** transitions in the 5.5−6.8 eV region are separated as follows. The S_1* population profile was already determined from the $D_0 \leftarrow S_1$* signal in the 3.0−5.5 eV region; therefore, it can be employed to estimate the $D_1 \leftarrow S_1$* time profile in the 5.5−6.8 eV region, except for its absolute intensity. The formation curve for the S_1** population must be the same as the decay curve for S_1* because the overall population in the S_1 manifold is maintained in this time range. Thus, what are unknown here are the relative ionization cross-sections for the $D_1 \leftarrow S_1$* and $D_0 \leftarrow S_1$** transitions and the decay time constant for S_1**. By assuming latency and rise times of 10 and 21 fs for S_1**, respectively, the decay time for S_1** was estimated to be 37 ± 2 fs. (As described in Supporting Information section S6-2, TRPEI estimates the lifetime of S_1** to be 27 ± 10 fs.) Figure 2D shows spectral features of the separated $D_1 \leftarrow S_1$* and $D_0 \leftarrow S_1$** bands (the details of the spectral fitting method are described in Supporting Information section S5). The intensity of the $D_1 \leftarrow S_1$* band is stronger than expected from the electron configuration shown in Table 1, for the reason explained later.

An important point raised by van der Lugt and Oosterhoff regarding the electrocyclic reaction is the involvement of the doubly excited state.[9] However, the character of each electronic state possibly varies with nuclear displacements so that one may ask whether the S_2** and S_1** states really have a doubly excited electronic character. It would be of interest to investigate this point using configuration interaction (CI) calculations in order to establish this concept more firmly. Figure 3A shows one-dimensional potential energy curves calculated for CHD using the extended multistate complete active space second-order perturbation theory (XMS-

https://doi.org/10.1021/jacs.1c01896
J. Am. Chem. Soc. XXXX, XXX, XXX−XXX

Table 1. Electronic Energies of CHD Calculated Using XMS-CASPT2 under C_2 Symmetry and Corresponding Experimental Values (eV)

	at 1^1A equilibrium geometry			at 2^1A equilibrium geometry	
state	leading configuration(s)	calcd	exptl	leading configuration(s)	calcd
3^2B	$(9b)^2(11a)^2(10b)^2(\mathbf{12a})^0(\mathbf{11b})^1$	11.78	11.8[a]	$(10a)^2(10b)^2(\mathbf{11a})^1(\mathbf{11b})^1(\mathbf{12a})^1$	13.72
2^2B	$(\mathbf{9b})^1(11a)^2(10b)^2(12a)^2(11b)^0$	11.60	11.8[b]	$(10a)^2(\mathbf{10b})^1(11a)^2(11b)^2(12a)^0$	13.09
				$(10a)^2(\mathbf{10b})^1(11a)^2(11b)^0(12a)^2$	
2^2A	$(9b)^2(\mathbf{11a})^1(10b)^2(12a)^2(11b)^0$	11.11	11.3[b]	$(10a)^2(10b)^2(\mathbf{11a})^1(11b)^2(12a)^0$	13.16
				$(10a)^2(10b)^2(\mathbf{11a})^1(11b)^0(12a)^2$	
1^2B	$(9b)^2(11a)^2(\mathbf{10b})^1(12a)^2(11b)^0$	10.70	10.7[b]	$(10a)^2(10b)^2(11a)^2(\mathbf{11b})^1(12a)^0$	9.98
1^2A	$(9b)^2(11a)^2(10b)^2(\mathbf{12a})^1(11b)^0$	8.37	8.25[b]	$(10a)^2(10b)^2(11a)^2(11b)^0(\mathbf{12a})^1$	10.00
2^1A	$(9b)^2(11a)^2(\mathbf{10b})^1(12a)^2(\mathbf{11b})^1$	6.06[c]		$(10a)^2(10b)^2(11a)^2(11b)^2(12a)^0$	3.80
	$(9b)^2(11a)^2(10b)^2(\mathbf{12a})^0(\mathbf{11b})^2$			$(10a)^2(10b)^2(11a)^2(11b)^0(12a)^2$	
	3s Rydberg state[d]	5.87[d]	5.39[e]		
1^1B	$(9b)^2(11a)^2(10b)^2(\mathbf{12a})^1(\mathbf{11b})^1$	4.88	4.94[f]	$(10a)^2(10b)^2(11a)^2(\mathbf{11b})^1(\mathbf{12a})^1$	4.21
1^1A	$(9b)^2(11a)^2(10b)^2(12a)^2(11b)^0$	0	0	$(10a)^2(10b)^2(11a)^2(11b)^2(12a)^0$	2.83
				$(10a)^2(10b)^2(11a)^2(11b)^0(12a)^2$	

[a]This work. The details of computational method are described in the Computational Simulation section. The absorption spectrum of the CHD cation in a freon matrix[25] suggests 11.5 eV. The 3^2B and 2^2B are almost degenerate, and their energetic orders are difficult to determine. [b]He I PES.[26] [c]Classified as 4^1A at the FC geometry. [d]The leading configuration is ...$(9b)^2(11a)^2(10b)^2(12a)^1(11b)^0(13a)^1$. The state energy was calculated in the multistate-multireference scheme of XMS-CASPT2 with an active space of four electrons in eight orbitals, namely, two π and two π^* orbitals in addition to 3s, $3p_x$, $3p_y$, and $3p_z$ Rydberg orbitals. 13*a* is of 3s Rydberg character. [e]Resonance enhanced multiphoton ionization.[27] [f]Optical and electron energy loss spectroscopies.[28]

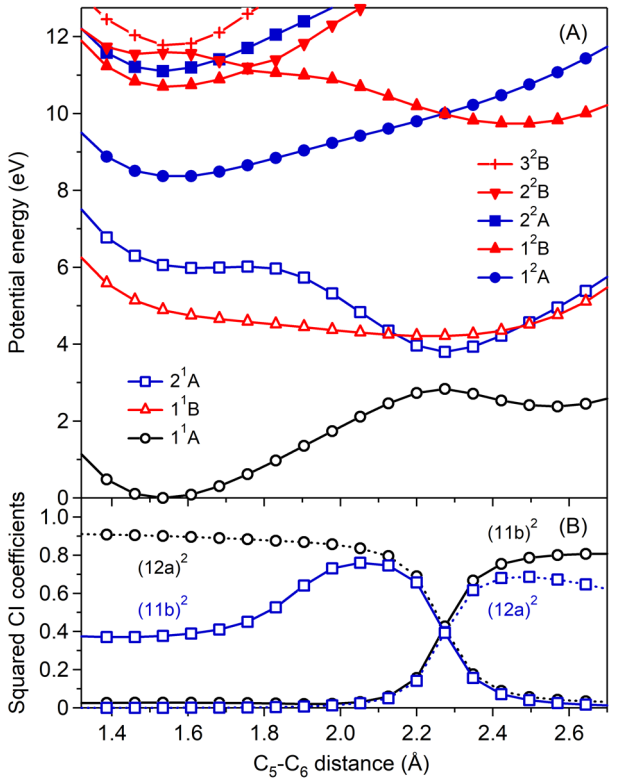

Figure 3. (A) Potential energy curves of 1^1A, 1^1B, 2^1A, 1^2A, 1^2B, 2^2A, 2^2B, and 3^2B for CHD calculated assuming C_2 symmetry. (B) Squared CI coefficients of the doubly excited configurations in the electronic wave functions of the 1^1A and 2^1A states.

CASPT2) method as a function of the C_5−C_6 distance by assuming that C_2 symmetry is maintained. Under C_2 symmetry, the $S_1(1^1B)$ and $S_2(2^1A)$ potential energy curves are crossed because they belong to different irreducible representations. On the other hand, the 2^1A and $S_0(1^1A)$ states form a strong avoided crossing at around a C_5−C_6 distance of 2.3 Å. Table 1 lists the leading electron configurations of these states for equilibrium geometries of 1^1A and 2^1A. It can be seen that the electronic character of $S_2(2^1A)$ in the ground-state equilibrium geometry contains a fair amount of $[(10b)^1(12a)^2(11b)^1]$ configuration in addition to the doubly excited configuration of $[(10b)^2(12a)^0(11b)^2]$. Is the fraction of the doubly excited character of 2^1A smaller than our expectation? In order to clarify this point further, we evaluated the fraction of the doubly excited characters of $[(10b)^2(12a)^0(11b)^2]$ and $[(10b)^2(12a)^2(11b)^0]$ in the electronic wave functions of 1^1A and 2^1A using the CI coefficients obtained using XMS-CASPT2 calculations. Figure 3B shows the squared CI coefficients of the doubly excited configurations in the electronic wave functions of the 1^1A and 2^1A states as a function of the C_5−C_6 distance. The results indicate that the $(11b)^2$ doubly excited character in the 2^1A state increases as the C_5−C_6 bond is elongated to 2.0 Å, where the 2^1A potential energy curve crosses the 1^1B curve. Thus, the calculations confirmed that the second valence-excited singlet state has a doubly excited electronic character near the S_2/S_1 surface crossing region. Since most of the nuclear trajectories from the Franck−Condon region to the S_2/S_1 minimum energy conical intersection (MECI) pass the region close to the C_2 symmetry, the above argument assuming C_2 symmetry is valid for an ensemble of nuclear trajectories in this region of the potential energy surface, even without the symmetry restriction assumed here.

Previously, this reaction has been studied using UV two-photon ionization from the excited state. Two-photon TRPES studies revealed the sequential appearance of resonance-enhanced two-photon ionization via Rydberg states from high to low principal quantum numbers (n);[5,19] however, the origin of these signals was not well understood. In order to revisit this problem, we performed two-photon UV-TRPEI with a higher time-resolution (58 fs) than in previous studies and obtained the results shown in Figure 4A. It is seen that the 6s Rydberg state has a maximum at a delay time of 13 fs, while the 3p state has a maximum at 35 fs. One of the key criteria for

https://doi.org/10.1021/jacs.1c01896
J. Am. Chem. Soc. XXXX, XXX, XXX−XXX

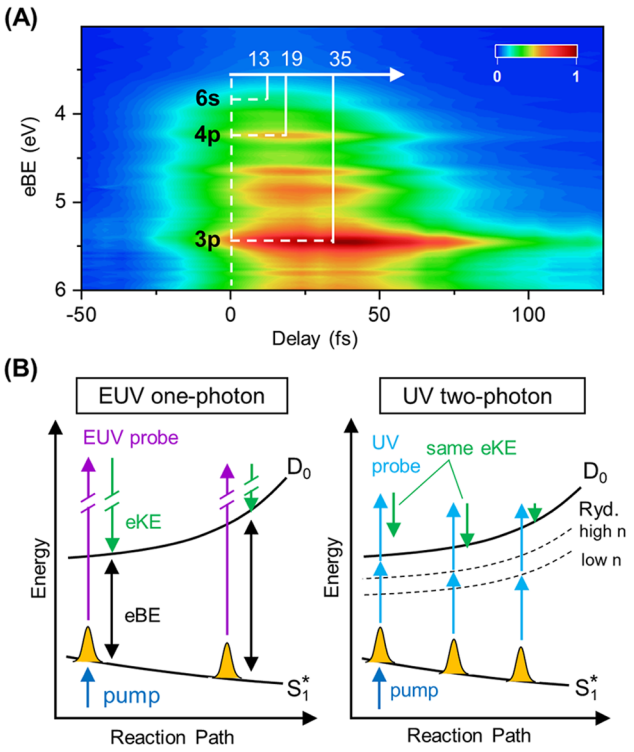

Figure 4. TRPES with two-photon ionization. (A) 2D map of the photoelectron spectra measured with the resonance-enhanced two-photon ionization via Rydberg states using 394 nm probe pulses. (B) Schematic diagram of photoionization from S_1* with EUV and UV probe pulses.

the assignment of these Rydberg signals is their appearance times; as the experimental results shown in Figure 2 revealed, the photoexcited CHD is in the S_1* state within this time range. Therefore, this clearly represents ionization from the S_1* state. It is noted that the energy difference between the Rydberg state and S_1* is expressed by

$$E_{\mathrm{Ryd}} - E(S_1^*) = \mathrm{eBE}(S_1^*) - R/(n-\delta)^2$$

where δ is a quantum defect and R is the Rydberg constant. Thus, the excitation energies from S_1* to the Rydberg series increases exactly with eBE(S_1*). We have already seen the rapid increase in eBE(S_1*) in Figure 2. Consequently, the Rydberg state in resonance with the UV probe photon energy progressively shifts to lower Rydberg states with decreasing values of $n - \delta$ (see Figure 4B). Presumably, part of the two-photon ionization via 3p Rydberg states after 30 fs is from S_1**.

In order to confirm our interpretation of the EUV photoelectron spectra and to gain further insight into the dynamics, we employed two theoretical analyses. In the first approach, we selected the most probable ring-opening reaction path estimated by geodesical interpolation[29] among the molecular geometries of FC, S_2/S_1 MECI, S_1/S_0 MECI (non-C_2-symmetry), and the equilibrium geometries of the HT isomers, and we calculated the eBE values and photoionization cross-sections along the path using the XMS-CASPT2 method, as shown in Figure 5A. The highest cationic state considered here is D_4. Superimposed with different colors in this figure are the ionization cross-sections estimated from the norm of Dyson orbitals. The value on the horizontal axis is the total arc length for nuclei to move along this reaction path so that the value extends up to 25 Å. A semilog plot is used here to present rather congested trajectories for different

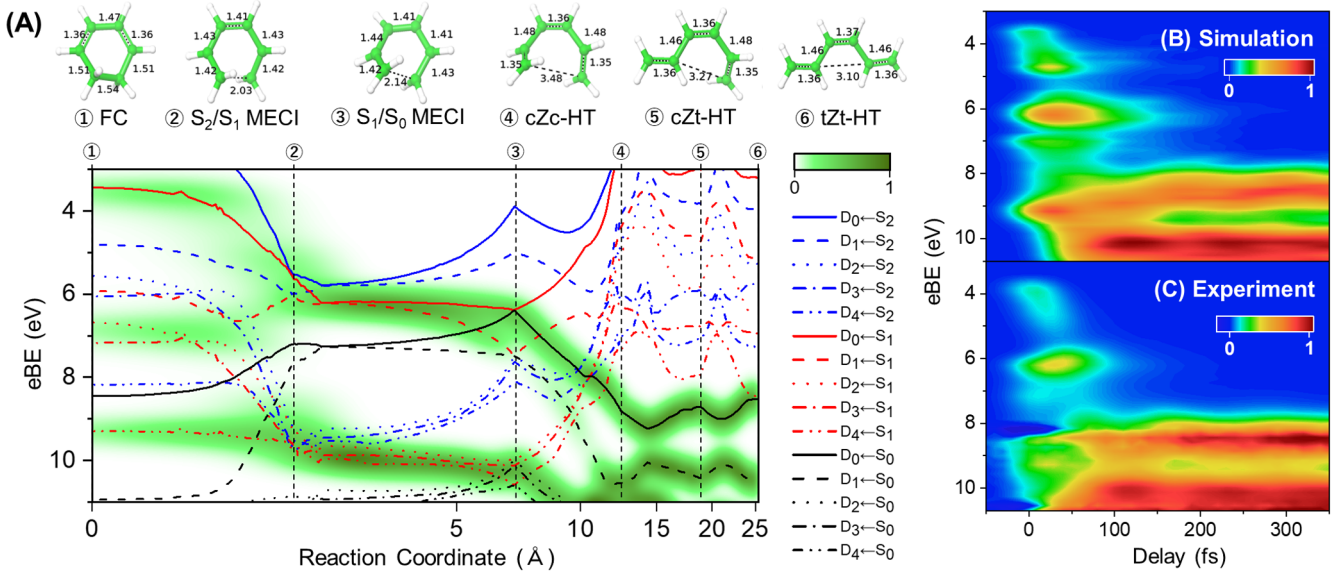

Figure 5. Computational simulation of photoelectron spectra. (A) Variation of eBE calculated along the geodesically interpolated ring-opening reaction path connecting the FC state, S_2/S_1 MECI, S_1/S_0 MECI, cZc, cZt, and tZt forms of HT. Ionization from S_0–S_2 to D_0–D_4 is considered. Photoionization cross-sections estimated from the norm of Dyson orbitals for each ionization channel are superimposed. The value on the horizontal axis, shown in a logarithmic scale, is the total arc length for nuclei to move along this reaction path. Molecular structures in FC, S_2/S_1 MECI, S_1/S_0 MECI and the S_0 minimum are illustrated on top with the bond length (Å). (B) Photoelectron spectra simulated based on trajectory surface hopping calculations by Polyak et al.[8] Both CHD and HT forming channels are included, and experimental temporal (48 fs) and energy (0.12 eV) resolutions are incorporated. (C) Experimental time energy map obtained by elimination of the ground-state bleach signal from the data shown in Figure 2A.

https://doi.org/10.1021/jacs.1c01896
J. Am. Chem. Soc. XXXX, XXX, XXX−XXX

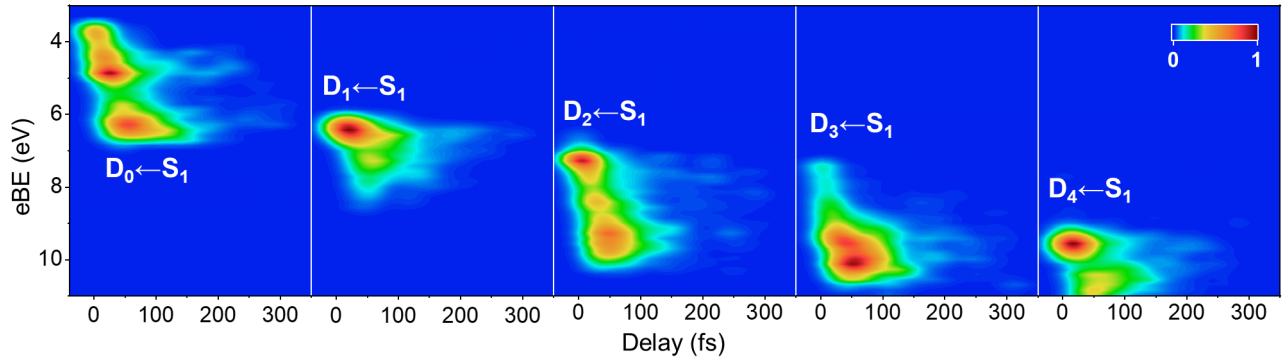

Figure 6. Photoelectron spectra due to transitions from S_1 state to different cationic states simulated based on trajectory surface hopping calculations by Polyak et al.[8] Experimental temporal (48 fs) and energy (0.12 eV) resolutions are incorporated.

ionization channels in the range of small displacement along the reaction path. The figure indicates a steep increase in the eBE value for the $D_0 \leftarrow S_1$* band, followed by a rather constant eBE value for $D_0 \leftarrow S_1$** and a large increase in eBE upon formation of the ground-state HT. These features are in excellent agreement with the experimental results shown in Figure 2. The eBE values calculated using the XMS-CASPT2 level of theory were highly accurate and in quantitative agreement with the experimental values; however, we found that the simulated spectra were being shifted by −0.4 eV with respect to the experimental ones. Therefore, we adjusted the simulated spectra by +0.4 eV for closer comparison with the experimental results. In order to relate the eBE values and the molecular structures, the calculated structures at the critical points along the reaction path are also shown in Figure 5A. The CHD molecule has two C═C double bonds in the FC geometry, while all carbon−carbon bonds except the dissociating C_5-C_6 become almost the same length in the structures for S_2/S_1 and S_1/S_0 CoIn. The equilibrium structures of HT isomers have three C═C double bonds. Greater structural change occurs on the ground-state surface of HT. The actual nuclear motions are not restricted to this geodesically interpolated path; therefore, the map shown in Figure 5A only describes the principal part of the multidimensional dynamics. Nonetheless, the one-dimensional analysis in Figure 5A provided highly valuable insights into the reaction and photoionization dynamics.

A clear limitation of the results shown in Figure 5A is that they do not include a nonreactive internal conversion path to the S_0 state of CHD or predict the reaction time. Therefore, in the second approach, we performed a thorough dynamical simulation of the experimental results by a combination of the full-dimensional surface hopping calculations performed by Polyak et al.[8] and our own calculations of the ionization dynamics at the XMS-CASPT2 level of theory. The spectra thus simulated are shown in Figure 5B, including both pathways to form CHD and HT. The highest cationic state considered in this simulation is D_4, and the simulated spectra are shifted by 0.4 eV as mentioned earlier. The experimental temporal (48 fs) and energy (0.12 eV) resolutions were incorporated. The simulated spectra are in excellent agreement with the experimental results shown in Figure 5C.

For closer examination of the photoelectron spectra, we present photoemission time−energy profiles for individual photoionization channels from the S_1 state to five cationic states of CHD in Figure 6. In these panels, S_1* and S_1** are not differentiated; however, the $D_0 \leftarrow S_1$* and $D_0 \leftarrow S_1$** transitions can clearly be seen in the panel for D_0-S_1. As described earlier, one puzzling feature concerning the experimentally observed $D_1 \leftarrow S_1$* band is that it appeared with a greater intensity than expected (Figure 2). Since the leading electron configurations for S_1* and D_1 are respectively $[(10b)^2(12a)^1(11b)^1]$ and $[(10b)^1(12a)^2(11b)^0]$ (see Table 1), the $D_1 \leftarrow S_1$* ionization transition is expected to be very weak; Figure 5A also predicts a low intensity for this transition in accordance with this expectation. However, examination of Figure 5B reveals that the spectral simulation based on the full-dimensional surface hopping trajectory calculations reproduces the strong appearance of the $D_1 \leftarrow S_1$* band. What is the reason for this difference? In order to find the origin of this enhanced ionization intensity, we examined the $D_1 \leftarrow S_1$* photoionization cross-section along the full-dimensional nuclear trajectories in the S_1* state. We found that the $D_1 \leftarrow S_1$* cross-section estimated from the Dyson norm is only 0.1 for the FC geometry, while it is 0.3 on average for an ensemble of trajectories spreading out from the FC geometry. Therefore, the higher intensity of the $D_1 \leftarrow S_1$* band is ascribed to a non-Condon effect due to variation of the electronic wave function caused by nuclear motions perpendicular to the ring-opening reaction coordinate.

Meanwhile, the leading electron configurations for S_2** and D_0 are $[(10b)^2(12a)^0(11b)^2] + [(10b)^1(12a)^2(11b)^1]$ and $[(10b)^2(12a)^1(11b)^0]$, respectively, in the ground-state equilibrium geometry; therefore, photoionization from S_2** to D_0 is unfavorable for this geometry. However, the leading electron configurations for S_1** and D_0 change to $[(11a)^2(11b)^2(12a)^0] + [(11a)^2(11b)^0(12a)^2]$ and $[(11a)^2(11b)^1(12a)^0]$ and/or $[(11a)^2(11b)^0(12a)^1]$ for the equilibrium geometry of S_1**, respectively. This enables a strong $D_0 \leftarrow S_1$** ionization transition. Examination of Figure 5A reveals that the $D_0 \leftarrow S_1$** band is overlapping with the $D_1 \leftarrow S_1$** band in the reaction coordinate range from 2 to 7 Å. These are basically transitions to the cationic 1^2A and 1^2B states. As seen in Figure 3A, the potential energy curves for S_1*(2^1A) and $D_0(1^2B)$ are nearly parallel to each other; therefore, the $D_0 \leftarrow S_1$** band exhibits a relatively constant eBE value.

Although the accuracy of the computational simulations presented in Figure 5B is among the highest reported, close comparison between the computational and experimental results reveals some discrepancies. First of all, the reaction time is slightly longer for the computational results, which points to small inaccuracies in the calculated potential energy surfaces. Second, the photoemission intensity for the excited

https://doi.org/10.1021/jacs.1c01896
J. Am. Chem. Soc. XXXX, XXX, XXX−XXX

states of CHD appears slightly stronger in the computational results, which suggests small inaccuracies in the ionization

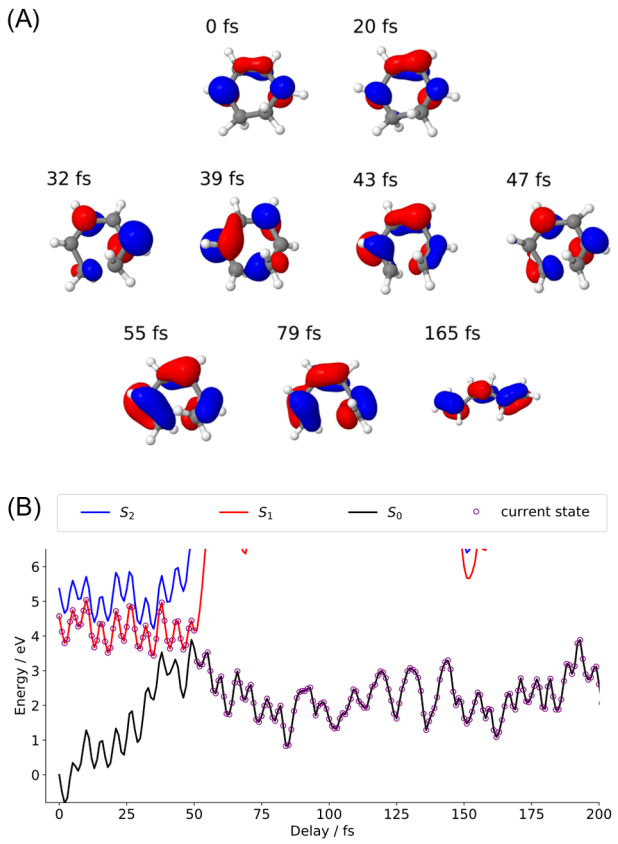

Figure 7. Representative trajectory leading to HT. (A) Snapshots of Dyson orbitals for ionization from current electronic state to D_0. (B) Electronic energies along nuclear trajectory, where current state is marked by purple circles.

cross-sections obtained from the Dyson norms. Third, the calculated photoemission bands are slightly shifted in energy from the experimental ones, as described earlier.

To understand the electronic and structural dynamics more clearly, Figures 7 and 8 present the time-evolution of the Dyson orbital, which can be regarded as an electron hole created by photoionization, and molecular geometry along the two nuclear trajectories leading to HT and CHD products, obtained using full-dimensional surface hopping calculations. In Figure 7A, it can be seen that the Dyson orbital associated with photoionization from S_1* at delay times of 0 and 20 fs is a 11b singly occupied molecular orbital. However, the 12a character with a node between the C_2 and C_3 carbon atoms emerges at 32 fs, and the Dyson orbital exhibits frustrated flickering until 50 fs when the 11b character dominates in the ground state of HT. In Figure 8A, the Dyson orbitals at 0 and 20 fs also have an 11b character, while at 27 fs it has a 12a character. The Dyson orbital at 55 fs is clearly 12a in the ground state of CHD. The important contributions of both the 11b and 12a orbitals seen here are consistent with Figure 3B. Using these Dyson orbitals, we will further discuss the notion of doubly excited state characters. The Dyson orbitals shown in Figures 7 and 9 clearly indicate that the S_1 and S_0 electronic wave functions in the avoided crossing region have equal 11b and 12a characters. A linear combination of 11b and 12a

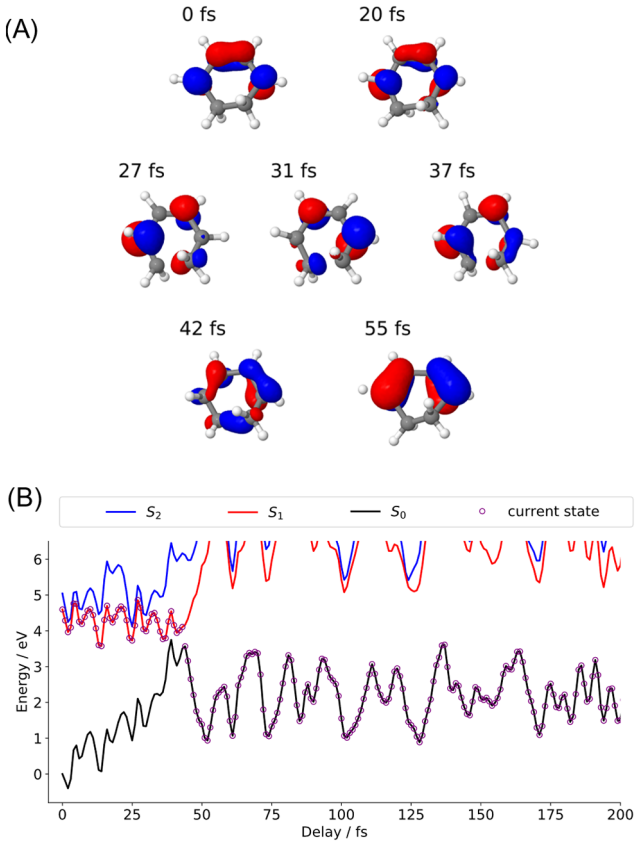

Figure 8. Representative trajectory leading to CHD. (A) Snapshots of Dyson orbitals for ionization from current electronic state to D_0. (B) Electronic energies along nuclear trajectory, where current state is marked by purple circles.

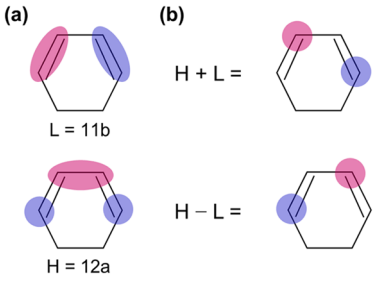

Figure 9. (a) 11b and 12a molecular orbitals (as in Figure 1). (b) Linear combination of 11b and 12a orbitals with equal amplitudes.

orbitals with equal weights creates the orbital patterns 12a + 11b and 12a − 11b, as shown in Figure 9, and these are clearly seen at delay times of 32 and 39 fs in Figure 7A. When we take these orbitals as the basis functions, the following relationship is obtained:

$$[(12a + 11b)^1(12a - 11b)^1] = [(12a)^2(11b)^0] - [(12a)^0(11b)^2]$$

Thus, the same electronic state can be expressed either with a singly excited electronic character with one basis (left) or with a doubly excited electronic character with the other basis (right). The aforementioned notion of a doubly excited state is based on the latter standpoint; it should be kept in mind that the description of the electronic wave function depends on the

https://doi.org/10.1021/jacs.1c01896
J. Am. Chem. Soc. XXXX, XXX, XXX−XXX

basis functions. The interesting features in Figures 7B and 8B are that the electronic energies for both CHD and HT

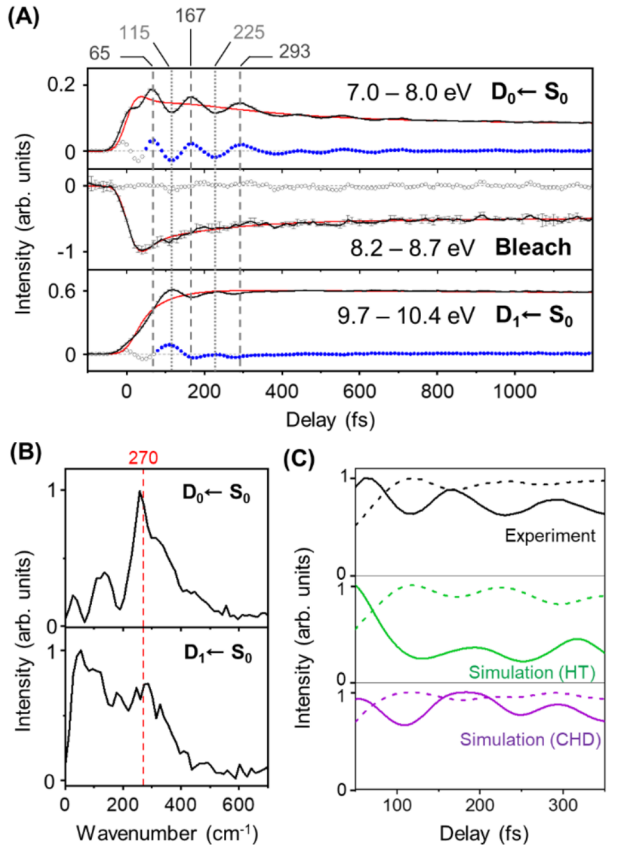

Figure 10. Vibrational coherence in reaction products. (A) Time profile of photoelectron intensities integrated over eBE regions of 7.0−8.0, 8.2−8.7, and 9.7−10.4 eV. Black lines are the experimental data, and red lines are the population obtained by the analysis described in section S3 of the Supporting Information. It is noted that the phase of the oscillations is shifted by π between the traces of 7.0−8.0 and 9.7−10.4 eV. The trace for 8.2−8.7 eV is for the photoelectron band center of the ground-state CHD, for which no oscillatory component is identified. (B) Fourier transform of oscillatory components in $D_0 \leftarrow S_0$ and $D_1 \leftarrow S_0$ transitions of the reaction products. Fourier components were obtained from the residues shown with blue dots in (A). A rectangular window function was used in the Fourier transform. (C) Comparison of the observed vibrational quantum beat and computed photoelectron intensities for CHD and HT products in selected eBE regions of 7.0−8.0 eV (solid line) and 9.7−10.4 eV (dashed line).

products vary between 1 and 3 eV, indicating that these trajectories do not sample the potential region near the ground-state equilibrium geometries of the products.

Returning to the photoelectron spectra in Figure 2A, it can be seen that the photoelectron signals from the nascent reaction products exhibit sinusoidal intensity modulation. These are vibrational coherence in the reaction products created by this ballistic ring-opening reaction. Figure 10A shows the time profiles of these photoelectron signal intensities integrated over selected eBE regions. The signals in the 7.0−8.0 and 9.7−10.4 eV regions exhibit clear intensity oscillations. Furthermore, the phase of the oscillation differs by π between these two regions. For comparison, the signal integrated for 8.2−8.7 eV is of the ground-state bleach of CHD, and it does not exhibit any oscillation. An intense pump pulse can generally induce impulsive Raman scattering to create vibrational coherence in the ground state of the reactant; however, the oscillatory features observed in the eBE region of 9.7−10.4 eV are well separated from the photoelectron bands of cold CHD (Figure 2A). Therefore, the observed beat signals are clearly of the vibrational coherence in the products (hot CHD or HT). We performed Fourier transform of these time profiles for the temporal region indicated with blue dots in Figure 10A, and we found the main quantum beat component was centered at 270 cm^{-1} in the unit of wavenumbers (see Figure 10B). We have measured similar data for a shorter pump wavelength of 250 nm and obtained essentially the same oscillatory features albeit with slightly smaller amplitudes (see Supporting Information section S4).

The definitive assignment of these quantum beats is difficult at this point. As shown in Figure 11, the photoelectron spectra

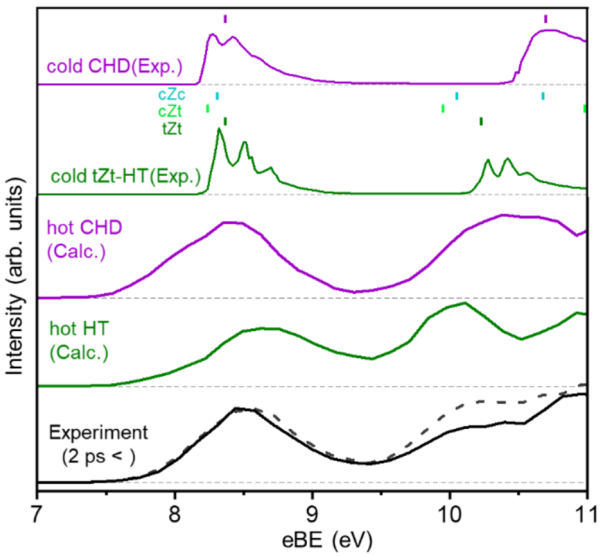

Figure 11. Photoelectron spectra of CHD and HT. (Top two panels) Experimental photoelectron spectra of CHD and HT(tZt)[26,34] measured at room temperature along with the band positions predicted using XMS-CASPT2 quantum chemical calculations. The calculated positions were not shifted. (Middle two panels) Photoelectron spectra of CHD and HT produced by the ring-opening reaction of CHD calculated using XMS-CASPT2 surface hopping calculations. The calculated spectra were shifted by +0.4 eV to compare with the experimental result. (Bottom panel) Experimental photoelectron spectrum of reaction products. Solid and dashed lines show the experimental results with pump pulses of 267 and 252 nm, respectively. The negative signals in the experimental spectrum due to the ground-state bleach of CHD were compensated by addition of the photoelectron spectrum of cold CHD with an estimated pumping efficiency.

of hot CHD and HT computed based on the aforementioned full-dimensional trajectory calculations and ionization cross-sections were quite similar to each other and their spectral separation was difficult. Alternatively, we examined the computed photoelectron spectra for CHD and HT and extracted the oscillatory features as shown in Figure 10C. Both of the calculated photoelectron spectra for CHD and HT products exhibit oscillatory features, although the amplitude was greater for HT. Therefore, the experimentally observed vibrational coherence is most likely of the HT product;

https://doi.org/10.1021/jacs.1c01896
J. Am. Chem. Soc. XXXX, XXX, XXX−XXX

however, quantum mechanical analysis is necessary for more definitive assignment in the future. An ultrafast electron diffraction study on this system[21] indicated an oscillatory feature of the diffraction signal of HT with an interval of 0.25 and 0.29 ps. The period of the vibrational quantum beat shown in Figure 10 is about 100 fs and ascribed to a different type of vibrational motion.

Vibrational coherence in the photochemical reaction product has been observed for the *cis*−*trans* photoisomerization of rhodopsin by Mathies and co-workers using stimulated Raman spectroscopy[30−32] and by Miller and co-workers using transient grating spectroscopy.[33] The product vibrational coherence observed in the ring-opening reaction of CHD is attributed to strong electronic coupling and an extremely short reaction time, which are similar to the case of rhodopsin.

SUMMARY

The present study firmly established the reaction pathway mediated by the doubly excited state for the paradigmatic ring-opening reaction of 1,3-cyclohexadiene and also uncovered its extremely short reaction time (68 ± 7 fs). Our estimate of the reaction time is based on the decay of the excited state of CHD, which corresponds to formation of the cZc form of HT. Formation of the tZt involves rotational isomerization around C−C single bonds, and it will be slightly delayed. The ultrashort reaction time is comparable with the *cis*−*trans* photoisomerization of retinal in rhodopsin for which product vibrational coherence has been observed.[30−33] The computed eBE map along the geodesically interpolated reaction pathway reproduced the general features of the experimental photoelectron spectra well, and the full-dimensional computational simulation of the photoelectron spectra based on the XMS-CASPT2 surface hopping dynamics calculation reproduced the experimental results semiquantitatively. Rigorous assignment of the observed vibrational quantum beat was difficult in the framework of this study, and it awaits more thorough quantum mechanical analysis of nuclear motions. At this point, we speculate that it is most likely of HT products. We estimated the photoelectron spectra of hot CHD and HT from the trajectory data and photoionization cross-sections and concluded that clear differentiation of the CHD and HT products is not feasible with photoelectron spectroscopy. For this reason, reliable experimental evaluation of the CHD/HT branching ratio in this reaction was difficult in the present study. Estimation of the branching ratio is expected to be possible with diffraction experiments.[35] The time-resolution of EUV photoelectron spectroscopy can be further improved by shortening the driving laser pulse duration[36] and the use of a time-compensated EUV monochromator;[37] the cross-correlation time of the laser system in the present study was predominantly determined by the temporal width of an EUV pulse. It is of great interest to explore various photochemical reactions using EUV-TRPES with a higher temporal resolution.

EXPERIMENTAL SECTION

Experimental Setup. A one-box 1 kHz Ti:sapphire regenerative amplifier (35 fs, 800 nm, 1 kHz, 6 mJ) was used as a driving laser for nonlinear optical processes to generate the DUV pump (267.5 nm) and EUV probe (57.1 nm) pulses. The probe pulses were produced using HHG in Kr gas with the second harmonic (2ω, 0.29 mJ) of the Ti:sapphire laser as a driving pulse.[22] The 2ω laser pulses were produced with a 0.3 mm thick β-barium borate crystal and focused using a quartz lens (f = 500 mm) into a Kr gas cell. The 14th order single harmonic (14ω: 57 nm, 21.7 eV) was selected with a grating-based time-preserving monochromator. The pump pulses were generated using FFWM in Ar gas using the fundamental (ω, 0.5 mJ) and 2ω (0.3 mJ) pulses.[24] The output pulses were reflected and monochromatized using multilayer mirrors designed for 3ω. The optical path length of the 3ω pulses was controlled using a translation stage with 5 nm resolution. The temporal width and energy of the pump pulses were sub-30 fs and 800 nJ/pulse, respectively. The cross-correlation time between the pump and probe pulses was determined to be 48 fs using nonresonant ionization of Xe.

CHD vapor seeded in He carrier was injected into a photoelectron spectrometer through a pinhole (⌀0.1 mm) at a stagnation pressure of 0.06 MPa at room temperature. The eKE distribution was measured using a magnetic bottle time-of-flight (TOF) spectrometer.[38] The photoelectrons traveled through a 1300 mm long flight tube were detected using a microchannel plate detector (⌀42 mm) at the end of the flight tube. A retardation voltage of −6.0 V was applied to the flight tube in order to reject low-energy electrons produced by one-color two-photon ionization of CHD with the pump pulses. The energy calibration of the photoelectron spectrometer was performed using the $^2P_{3/2}$ and $^2P_{1/2}$ peaks in the photoelectron spectrum of Xe. The energy resolution was estimated to be 0.12 eV. The pressure in the photoionization chamber and TOF analyzer was 4.0×10^{-5} and $<1.0 \times 10^{-7}$ Torr, respectively, during the measurements. Further information on the experimental setup is described in the Supporting Information section S1.

Computational Simulation. The ring-opening reaction of CHD proceeds by breaking its C_2 symmetry. However, the potential energy curves calculated under C_2 symmetry provide information regarding the correlation of the electronic states between CHD and HT. The effective potential energy curves for the ring-opening reaction of CHD were computed using the Roos atomic natural orbital (ANO) basis set[39] contracted to 4s3p2d functions for carbon and 2s1p functions for hydrogen using the ab initio quantum chemistry software MOLPRO.[40,41] For neutral CHD, static electron correlation was treated at the complete-active-space self-consistent field (CASSCF) level of theory[42,43] with an active space composed of six electrons distributed among six orbitals, i.e., two π and two π^* orbitals in addition to one σ and one σ^* orbital initially localized at the breaking C_5−C_6 bond. The CASSCF orbitals were averaged over the states of interest (1^1A, 1^1B, and 2^1A) with equal weights. Dynamic electron correlation was then taken into account at the level of the extended multistate CAS second-order perturbation theory (XMS-CASPT2)[44,45] with a level shift of 0.3 hartree adopted to avoid intruder state problems.[46] The geometry of CHD was optimized in the 1^1A and 2^1A states under C_2 symmetry constraints. Along the path linearly connecting the two optimized geometries, the three neutral states were evaluated using the multistate multireference (MS-MR) scheme of XMS-CASPT2. A number of cationic states accessible from the neutral states by a 21.7 eV photon were also obtained using the single-state single-reference (SS-SR) scheme of XMS-CASPT2 with a larger active space of thirty-one electrons in seventeen (fourteen σ, two π, and one π^*) orbitals. The results thus obtained are presented in Figure 3 and Table 1.

The ionization energies (vertical eBEs) for three isomers of cold HT, shown in Figure 11, were computed in a similar manner. The geometry optimization of neutral HT in the 1^1A state was conducted at the CASPT2 level with an active space consisting of six electrons in six (three π and three π^*) orbitals. The resultant equilibrium geometries of the cZc, cZt, and tZt isomers were of C_2, C_1, and C_{2v} symmetry, respectively. Cationic states reachable from the 1^1A state for each isomer were evaluated using the SS-SR scheme of XMS-CASPT2 with an active space of thirty-one electrons in seventeen (thirteen σ, three π, and one π^*) orbitals.

For simulations of photoelectron spectra shown in Figures 5−8, we evaluated the electronic structures of CHD and HT in a similar manner as that used by Polyak et al.[8] For singlet (doublet) cases, the XMS-CASPT2/cc-pVDZ calculations with an active space of eight (seven) electrons in eight orbitals were performed including the S_0−S_2 (D_0−D_4) states with the BAGEL[47] software. An energy shift of 0.5

https://doi.org/10.1021/jacs.1c01896
J. Am. Chem. Soc. XXXX, XXX, XXX−XXX

hartree was introduced. The photoionization cross-section was estimated from the norm of the Dyson orbitals, i.e., the overlap between CASPT2 wave functions for the initial (S_i) and the final (D_f) states, by neglecting the dependence on the electronic continuum. Dyson orbitals were computed with the help of a recent implementation by one of the authors (A.H.) in a development version of BAGEL. The molecular orbitals in the S_i and D_f wave functions differ due to orbital relaxation and are therefore non-orthogonal. The Dyson orbitals between Slater determinants built from nonorthogonal orbitals were evaluated as previously described.[48] The calculated energy structures of the cation are slightly different between Figures 3 and 5 owing to the difference in the active space considered in the calculations.

The minimum energy path that led to different isomers of HT in the ring-opening reaction of CHD was calculated at the XMS-CASPT2/cc-pVDZ level of theory. The reaction path from the FC region in S_1 through S_2/S_1 and S_1/S_0 MECIs to cZc, cZt, and tZt-HT was considered. The stationary points and MECIs were optimized,[49] and the intermediate segments joining these points were calculated by geodesic interpolation using a previously presented algorithm.[29] The time-resolved photoelectron spectra were calculated using previously obtained trajectory data (geometries and current electronic states).[8] The eBE values and Dyson norms were computed for ionization from each S_i to five D_f states along each trajectory with a time interval of 1 fs. The contributions from all trajectories were summarized in a 2D map and convoluted with the instrumental function for comparison with the experimental data.

■ ASSOCIATED CONTENT

Supporting Information

The Supporting Information is available free of charge at https://pubs.acs.org/doi/10.1021/jacs.1c01896.

Further information on experimental methods, analysis of the TRPES data, results of TRPEI experiments, and computational simulations (PDF)

■ AUTHOR INFORMATION

Corresponding Author

Toshinori Suzuki − *Department of Chemistry, Graduate School of Science, Kyoto University, Kyoto 606-8502, Japan;* orcid.org/0000-0002-4603-9168; Email: suzuki@kuchem.kyoto-u.ac.jp

Authors

Shutaro Karashima − *Department of Chemistry, Graduate School of Science, Kyoto University, Kyoto 606-8502, Japan*

Alexander Humeniuk − *Institut für Physikalische und Theoretische Chemie, Universität Würzburg, Würzburg 97074, Germany*

Ryuta Uenishi − *Department of Chemistry, Graduate School of Science, Kyoto University, Kyoto 606-8502, Japan*

Takuya Horio − *Department of Chemistry, Graduate School of Science, Kyoto University, Kyoto 606-8502, Japan;* Present Address: T.H.: Department of Chemistry, Faculty of Science, Kyushu University, 744 Motooka, Nishi-ku, Fukuoka 819-0395, Japan.

Manabu Kanno − *Department of Chemistry, Graduate School of Science, Tohoku University, Sendai 980-8578, Japan;* orcid.org/0000-0003-4701-906X

Tetsuro Ohta − *Department of Chemistry, Graduate School of Science, Kyoto University, Kyoto 606-8502, Japan*

Junichi Nishitani − *Department of Chemistry, Graduate School of Science, Kyoto University, Kyoto 606-8502, Japan*

Roland Mitrić − *Institut für Physikalische und Theoretische Chemie, Universität Würzburg, Würzburg 97074, Germany;* orcid.org/0000-0002-4941-0436

Complete contact information is available at: https://pubs.acs.org/10.1021/jacs.1c01896

Funding

This research was supported by JSPS KAKENHI Grant 15H05753, Mitsubishi Foundation, and the Japan-Belgium Research Cooperative Program between JSPS and F.R.S.-FNRS Grant JSBP120192201.

Notes

The authors declare no competing financial interest.

■ ACKNOWLEDGMENTS

The authors thank Dr. I Polyak and Professor P. J. Knowles for generously making the results of their surface hopping trajectory calculations available for comparison with our experimental results. M.K. gratefully acknowledges fruitful discussions with Professor F. Remacle and Dr. B. Mignolet on electronic structure computations.

■ REFERENCES

(1) Deb, S.; Weber, P. M. The ultrafast pathway of photon-induced electrocyclic ring-opening reactions: The case of 1,3-cyclohexadiene. *Annu. Rev. Phys. Chem.* **2011**, *62*, 19−39.

(2) Woodward, R. B.; Hoffmann, R. *The Conservation of Orbital Symmetry*; Verlag Chemie, 1969; Vol. *8*, pp 781−932.

(3) Garavelli, M.; Page, C. S.; Celani, P.; Olivucci, M.; Schmid, W. E.; Trushin, S. A.; Fuss, W. Reaction path of a sub-200 fs photochemical electrocyclic reaction. *J. Phys. Chem. A* **2001**, *105* (18), 4458−4469.

(4) Tamura, H.; Nanbu, S.; Ishida, T.; Nakamura, H. Ab initio nonadiabatic quantum dynamics of cyclohexadiene/hexatriene ultrafast photoisomerization. *J. Chem. Phys.* **2006**, *124* (8), 084313.

(5) Schalk, O.; Geng, T.; Thompson, T.; Baluyot, N.; Thomas, R. D.; Tapavicza, E.; Hansson, T. Cyclohexadiene revisited: A time-resolved photoelectron spectroscopy and ab initio study. *J. Phys. Chem. A* **2016**, *120* (15), 2320−2329.

(6) Lei, Y. B.; Wu, H. Y.; Zheng, X. L.; Zhai, G. H.; Zhu, C. Y. Photo-induced 1,3-cyclohexadiene ring opening reaction: Ab initio on-the-fly nonadiabatic molecular dynamics simulation. *J. Photochem. Photobiol. A* **2016**, *317*, 39−49.

(7) Ohta, A.; Kobayashi, O.; Danielache, S. O.; Nanbu, S. Nonadiabatic ab initio molecular dynamics of photoisomerization reaction between 1,3-cyclohexadiene and 1,3,5-cis-hexatriene. *Chem. Phys.* **2015**, *459*, 45−53.

(8) Polyak, I.; Hutton, L.; Crespo-Otero, R.; Barbatti, M.; Knowles, P. J. Ultrafast photoinduced dynamics of 1,3-cyclohexadiene using XMS-CASPT2 surface hopping. *J. Chem. Theory Comput.* **2019**, *15* (7), 3929−3940.

(9) van der Lugt, W. T. A. M.; Oosterhoff, L. J. Quantum-chemical interpretation of photo-induced electrocyclic reactions. *Chem. Commun.* **1968**, No. 20, 1235−1236.

(10) Nenov, A.; Kölle, P.; Robb, M. A.; de Vivie-Riedle, R. Beyond the van der Lugt/Oosterhoff model: When the conical intersection seam and the S_1 minimum energy path do not cross. *J. Org. Chem.* **2010**, *75* (1), 123−129.

(11) Kosma, K.; Trushin, S. A.; Fuß, W.; Schmid, W. E. Cyclohexadiene ring opening observed with 13 fs resolution: Coherent oscillations confirm the reaction path. *Phys. Chem. Chem. Phys.* **2009**, *11* (1), 172−181.

(12) Fuß, W.; Schmid, W. E.; Trushin, S. A. Time-resolved dissociative intense-laser field ionization for probing dynamics: Femtosecond photochemical ring opening of 1,3-cyclohexadiene. *J. Chem. Phys.* **2000**, *112* (19), 8347−8362.

(13) Mori, T.; Kato, S. Dynamic electron correlation effect on conical intersections in photochemical ring-opening reaction of cyclohexadiene: MS-CASPT2 study. *Chem. Phys. Lett.* **2009**, *476* (1−3), 97−100.
(14) Schönborn, J. B.; Sielk, J.; Hartke, B. Photochemical ring-opening of cyclohexadiene: Quantum wavepacket dynamics on a global ab initio potential energy surface. *J. Phys. Chem. A* **2010**, *114* (12), 4036−4044.
(15) Tudorovskaya, M.; Minns, R. S.; Kirrander, A. Effects of probe energy and competing pathways on time-resolved photoelectron spectroscopy: The ring-opening of 1,3-cyclohexadiene. *Phys. Chem. Chem. Phys.* **2018**, *20* (26), 17714−17726.
(16) Filatov, M.; Min, S. K.; Kim, K. S. Non-adiabatic dynamics of ring opening in cyclohexa-1,3-diene described by an ensemble density-functional theory method. *Mol. Phys.* **2019**, *117* (9−12), 1128−1141.
(17) Minitti, M. P.; Budarz, J. M.; Kirrander, A.; Robinson, J. S.; Ratner, D.; Lane, T. J.; Zhu, D.; Glownia, J. M.; Kozina, M.; Lemke, H. T.; Sikorski, M.; Feng, Y.; Nelson, S.; Saita, K.; Stankus, B.; Northey, T.; Hastings, J. B.; Weber, P. M. Imaging molecular motion: Femtosecond X-ray scattering of an electrocyclic chemical reaction. *Phys. Rev. Lett.* **2015**, *114* (25), 255501.
(18) Adachi, S.; Sato, M.; Suzuki, T. Direct observation of ground-state product formation in a 1,3-cyclohexadiene ring-opening reaction. *J. Phys. Chem. Lett.* **2015**, *6* (3), 343−346.
(19) Pemberton, C. C.; Zhang, Y.; Saita, K.; Kirrander, A.; Weber, P. M. From the (1B) spectroscopic state to the photochemical product of the ultrafast ring-opening of 1,3-cyclohexadiene: A spectral observation of the complete reaction path. *J. Phys. Chem. A* **2015**, *119* (33), 8832−8845.
(20) Attar, A. R.; Bhattacherjee, A.; Pemmaraju, C. D.; Schnorr, K.; Closser, K. D.; Prendergast, D.; Leone, S. R. Femtosecond X-ray spectroscopy of an electrocyclic ring-opening reaction. *Science* **2017**, *356* (6333), 54−59.
(21) Wolf, T. J. A.; Sanchez, D. M.; Yang, J.; Parrish, R. M.; Nunes, J. P. F.; Centurion, M.; Coffee, R.; Cryan, J. P.; Guhr, M.; Hegazy, K.; Kirrander, A.; Li, R. K.; Ruddock, J.; Shen, X.; Vecchione, T.; Weathersby, S. P.; Weber, P. M.; Wilkin, K.; Yong, H.; Zheng, Q.; Wang, X. J.; Minitti, M. P.; Martinez, T. J. The photochemical ring-opening of 1,3-cyclohexadiene imaged by ultrafast electron diffraction. *Nat. Chem.* **2019**, *11* (6), 504−509.
(22) Nishitani, J.; Yamamoto, Y.; West, C. W.; Karashima, S.; Suzuki, T. Binding energy of solvated electrons and retrieval of true UV photoelectron spectra of liquids. *Sci. Adv.* **2019**, *5* (8), eaaw6896.
(23) Pathak, S.; Ibele, L. M.; Boll, R.; Callegari, C.; Demidovich, A.; Erk, B.; Feifel, R.; Forbes, R.; Di Fraia, M.; Giannessi, L.; Hansen, C. S.; Holland, D. M. P.; Ingle, R. A.; Mason, R.; Plekan, O.; Prince, K. C.; Rouzee, A.; Squibb, R. J.; Tross, J.; Ashfold, M. N. R.; Curchod, B. F. E.; Rolles, D. Tracking the ultraviolet-induced photochemistry of thiophenone during and after ultrafast ring opening. *Nat. Chem.* **2020**, *12* (9), 795−800.
(24) Fuji, T.; Horio, T.; Suzuki, T. Generation of 12 fs deep-ultraviolet pulses by four-wave mixing through filamentation in neon gas. *Opt. Lett.* **2007**, *32* (17), 2481−2483.
(25) Honda, Y.; Shida, T.; Nakatsuji, H. Excitation spectra of cation and anion radicals of several unsaturated hydrocarbons: Symmetry adapted cluster-configuration interaction theoretical study. *J. Phys. Chem. A* **2012**, *116* (48), 11833−11845.
(26) Kimura, K.; Katsumata, S.; Achiba, Y.; Yamazaki, T.; Iwata, S. *Handbook of HeI Photoelectron Spectra of Fundamental Organic Molecules*; Japan Scientific Societies Press, 1981; p 68.
(27) Merchán, M.; Serrano-Andrés, L.; Slater, L. S.; Roos, B. O.; McDiarmid, R.; Xing, X. Electronic spectra of 1,4-cyclohexadiene and 1,3-cyclohexadiene: A combined experimental and theoretical investigation. *J. Phys. Chem. A* **1999**, *103* (28), 5468−5476.
(28) McDiarmid, R.; Sabljić, A.; Doering, J. P. Valence transitions in 1,3-cyclopentadiene, 1,3-cyclohexadiene, and 1,3-cycloheptadiene. *J. Chem. Phys.* **1985**, *83* (5), 2147−2152.
(29) Zhu, X.; Thompson, K. C.; Martinez, T. J. Geodesic interpolation for reaction pathways. *J. Chem. Phys.* **2019**, *150* (16), 164103.
(30) Schoenlein, R. W.; Peteanu, L. A.; Mathies, R. A.; Shank, C. V. The first step in vision: femtosecond isomerization of rhodopsin. *Science* **1991**, *254* (5030), 412−415.
(31) Kukura, P.; McCamant, D. W.; Yoon, S.; Wandschneider, D. B.; Mathies, R. A. Structural observation of the primary isomerization in vision with femtosecond-stimulated Raman. *Science* **2005**, *310* (5750), 1006−1009.
(32) Schnedermann, C.; Yang, X.; Liebel, M.; Spillane, K. M.; Lugtenburg, J.; Fernández, I.; Valentini, A.; Schapiro, I.; Olivucci, M.; Kukura, P.; Mathies, R. A. Evidence for a vibrational phase-dependent isotope effect on the photochemistry of vision. *Nat. Chem.* **2018**, *10* (4), 449−455.
(33) Johnson, P. J. M.; Halpin, A.; Morizumi, T.; Prokhorenko, V. I.; Ernst, O. P.; Miller, R. J. D. Local vibrational coherences drive the primary photochemistry of vision. *Nat. Chem.* **2015**, *7* (12), 980−986.
(34) Beez, M.; Bieri, G.; Bock, H.; Heilbronner, E. The ionization potentials of butadiene, hexatriene, and their methyl derivatives: Evidence for through space interaction between double-bond π-orbitals and non-bonded pseudo-π orbitals of methyl groups? *Helv. Chim. Acta* **1973**, *56* (3), 1028−1046.
(35) Ruddock, J. M.; Yong, H. W.; Stankus, B.; Du, W. P.; Goff, N.; Chang, Y.; Odate, A.; Carrascosa, A. M.; Bellshaw, D.; Zotev, N.; Liang, M. N.; Carbajo, S.; Koglin, J.; Robinson, J. S.; Boutet, S.; Kirrander, A.; Minitti, M. P.; Weber, P. M. A deep UV trigger for ground-state ring-opening dynamics of 1,3-cyclohexadiene. *Sci. Adv.* **2019**, *5* (9), eaax6625.
(36) Cheng, Y. C.; Lu, C. H.; Lin, Y. Y.; Kung, A. H. Supercontinuum generation in a multi-plate medium. *Opt. Express* **2016**, *24* (7), 7224−7231.
(37) Poletto, L.; Villoresi, P.; Benedetti, E.; Ferrari, F.; Stagira, S.; Sansone, G.; Nisoli, M. Intense femtosecond extreme ultraviolet pulses by using a time-delay-compensated monochromator. *Opt. Lett.* **2007**, *32* (19), 2897−2899.
(38) Kruit, P.; Read, F. H. Magnetic-field parallelizer for 2π electron-spectrometer and electron-image magnifier. *J. Phys. E: Sci. Instrum.* **1983**, *16* (4), 313−324.
(39) Widmark, P.-O.; Malmqvist, P.-Å.; Roos, B. O. Density matrix averaged atomic natural orbital (ANO) basis sets for correlated molecular wave functions. *Theor. Chim. Acta* **1990**, *77*, 291−306.
(40) Werner, H.-J.; Knowles, P. J.; Knizia, G.; Manby, F. R.; Schütz, M. Molpro: A general-purpose quantum chemistry program package. *Wiley Interdisp. Rev. Comput. Mol. Sci.* **2012**, *2* (2), 242−253.
(41) Werner, H.-J.; Knowles, P. J.; Knizia, G.; Manby, F. R.; Schütz, M.; Celani, P.; Korona, T.; Lindh, R.; Mitrushenkov, A.; Rauhut, G.; Shamasundar, K. R.; Adler, T. B.; Amos, R. D.; Bernhardsson, A.; Berning, A.; Cooper, D. L.; Deegan, M. J. O.; Dobbyn, A. J.; Eckert, F.; Goll, E.; Hampel, C.; Hesselmann, A.; Hetzer, G.; Hrenar, T.; Jansen, G.; Köppl, C.; Liu, Y.; Lloyd, A. W.; Mata, R. A.; May, A. J.; McNicholas, S. J.; Meyer, W.; Mura, M. E.; Nicklass, A.; O'Neill, D. P.; Palmieri, P.; Peng, D.; Pflüger, K.; Pitzer, R.; Reiher, M.; Shiozaki, T.; Stoll, H.; Stone, A. J.; Tarroni, R.; Thorsteinsson, T.; Wang, M. *MOLPRO*, version 2012.1; Cardiff, U.K., 2012.
(42) Werner, H. J.; Knowles, P. J. A second order multiconfiguration SCF procedure with optimum convergence. *J. Chem. Phys.* **1985**, *82* (11), 5053−5063.
(43) Knowles, P. J.; Werner, H.-J. An efficient second-order MC SCF method for long configuration expansion. *Chem. Phys. Lett.* **1985**, *115* (3), 259−267.
(44) Werner, H.-J. Third-order multireference perturbation theory The CASPT3 method. *Mol. Phys.* **1996**, *89* (2), 645−661.
(45) Shiozaki, T.; Győrffy, W.; Celani, P.; Werner, H.-J. Communication: Extended multi-state complete active space second-order perturbation theory: Energy and nuclear gradients. *J. Chem. Phys.* **2011**, *135* (8), 081106.

https://doi.org/10.1021/jacs.1c01896
J. Am. Chem. Soc. XXXX, XXX, XXX−XXX

(46) Roos, B. O.; Andersson, K. Multiconfigurational perturbation theory with level shift the Cr_2 potential revisited. *Chem. Phys. Lett.* **1995**, *245* (2−3), 215−223.
(47) BAGEL, Brilliantly Advanced General Electronic-structure Library. http://www.nubakery.org (accessed May 7, 2021), under the GNU General Public License.
(48) Humeniuk, A.; Wohlgemuth, M.; Suzuki, T.; Mitrić, R. Time-resolved photoelectron imaging spectra from non-adiabatic molecular dynamics simulations. *J. Chem. Phys.* **2013**, *139* (13), 134104.
(49) Bearpark, M. J.; Robb, M. A.; Schlegel, H. B. A direct method for the location of the lowest energy point on a potential surface crossing. *Chem. Phys. Lett.* **1994**, *223* (3), 269−274.

https://doi.org/10.1021/jacs.1c01896
J. Am. Chem. Soc. XXXX, XXX, XXX−XXX